Supporting Information

Planar ReN_1S_1 Sites with Dual σ-Channels Drive High-Performance CO_2 Photoreduction

Hao Sheng,[a] Shaokui Chen,[b] Guocheng Huang, [a] Jialong Lv,[a] Guiting Huang,[a] Wenjun Yang,[a] Ziyan Chen,[a] Shaoyu Wu,[a] Yueling Chen[ac*] and Jinhong Bi[ac*]

[a] *Department of Environmental Science and Engineering, Fuzhou University, Minhou, Fujian 350108, China*

[b] *Department of Materials Science and Engineering, Fuzhou University, Minhou, Fujian 350108, China*

[c] *State Key Laboratory of Photocatalysis on Energy and Environment, Fuzhou University, Minhou, Fujian 350108, China*

** Corresponding authors*

*E-mail address: 221310035@fzu.edu.cn (Y. Chen), bijinhong@fzu.edu.cn (J. Bi).

Characterization

Powder X-ray diffraction (PXRD) patterns were collected using Rigaku MiniFlex 600 X-ray diffractometer. Fourier transform infrared (FT-IR) spectra were acquired on Thermo Scientific Nicolet iS10 spectrometer. The ^{13}C nuclear magnetic resonance (^{13}C NMR), ^{1}H nuclear magnetic resonance (^{1}H NMR) and X-ray photoelectron spectroscopy (XPS) experiments were carried out on Bruker Avance III 500 and PHI Quantum 2000 XPS system, respectively. All binding energies were referenced to the C 1s peak (284.6 eV) of the surface adventitious carbon. The Brunauer-Emmett-Teller (BET) surface areas were determined by an ASAP 2020 apparatus (Micromeritics Instrument Corp.). Scanning electron microscopy (SEM) and high-resolution transmission electron microscopy (TEM) analyses were carried out by Nova Nano SEM 230 microscopy (FEI Corp.) and Tecnai G2 F20 microscope (FEI Corp.). The aberration-corrected high-angle annular dark-field scanning transmission electron microscopy (AC-HAADF-STEM) was performed with FEI Theims Z. Inductively coupled plasma atomic emission spectroscopy (ICP-AES) analysis was applied to measure the real loading amount of Re in catalysts on ICAP XSERIES2. The UV-vis diffuse reflectance spectroscopy (UV-vis DRS) was determined on Agilent Cary 5000 UV-Vis-NIR spectrophotometer using $BaSO_4$ as a reference. The photoelectrochemical measurements were measured using a conventional three-electrode system, where platinum plate and Ag/AgCl electrode were counter and reference electrode, respectively. The working electrode was prepared by depositing 10 μL of a thoroughly mixed suspension containing 5 mg catalyst and 0.5 mL ethanol onto a Fluoride-doped oxide (FTO) glass substrate (0.25 cm^2), with the exposed area covered with epoxy and then dried at room temperature. Mott-Schottky measurements and Electrochemical impedance spectroscopy (EIS) analyses were performed using a ZAHNER IM6 electrochemical workstation, with 0.2 mol·L^{-1} Na_2SO_4 aqueous solution and a mixed aqueous electrolyte of 5 mmol·L^{-1} $K_3[Fe(CN)_6]$/5 mmol·L^{-1} $K_4[Fe(CN)_6]$/0.1 mol·L^{-1} KCl employed for the two tests, respectively. Photocurrent measurements were recorded using a CHI650E electrochemical workstation in 0.2 mol·L^{-1} Na_2SO_4 aqueous solution, under irradiation with a 300 W Xe lamp equipped with a 420 nm cutoff filter. Room-temperature Photoluminescence (PL) spectra were collected using an Edinburgh FL/FS900 spectrophotometer (excitation wavelength: 420 nm). The E_b was calculated by fitting the integrated PL emission as a function of temperature according to Arrhenius equation, i.e., $I(T) = I_0/(1 + A \exp(-E_b/k_BT))$. Temperature-dependent photoluminescence (TDPL) spectra and time-resolved photoluminescence (TRPL) decay spectroscopy were retrieved with a FLS1000 under 420 nm pulsed laser-diode excitation. The linear sweep voltammetry (LSV) curves were measured using a ZAHNER IM6 electrochemical workstation in 0.2 mol·L^{-1} Na_2SO_4 aqueous solution; Ar was continuously bubbled into the electrolyte to maintain either an Ar-saturated or CO_2-saturated environment. CO_2 temperature-programmed desorption (CO_2-TPD) experiments were conducted on an AutoChem II analyzer (Micromeritics Instrument Corp.), with the temperature gradually increasing to 250 ℃ at a ramping rate of 10 ℃ min^{-1}. *In situ* Fourier transform infrared (*in situ* FT-IR) spectroscopy measurements were performed using a Thermo Scientific Nicolet iS10 spectrometer.

Theoretical calculations

The HOMO and LUMO orbital diagrams and electrostatic potential (ESP) analyses were obtained using Multiwfn program and visualized using Visual Molecular Dynamics (VMD, version 1.9.3, available at: http://www.ks.uiuc.edu/Research/vmd/) program. The density functional theory (DFT) calculations were performed using the Vienna Ab initio Simulation Package (VASP 5.4). A plane-wave basis set with an energy cutoff of 420 eV was employed, and the Gaussian smearing width was set to 0.2 eV. The Brillouin zone was sampled using a 3 × 3 × 1 K points. All atomic structures were relaxed until the force convergence criterion of 0.01 eV·$Å^{-1}$ was satisfied.

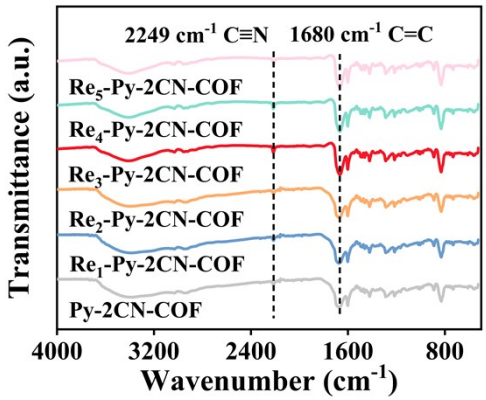

Fig. S1. The FT-IR spectra of Py-2CN-COF and Re_x-Py-2CN-COF (x=1, 2, 3, 4, 5).

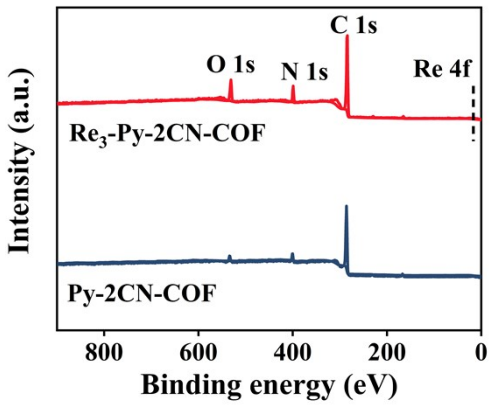

Fig. S2. The XPS survey spectrum for Py-2CN-COF and Re_3-Py-2CN-COF.

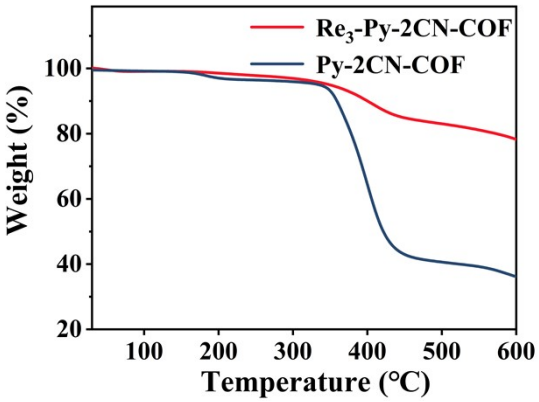

Fig. S3. The TGA of Py-2CN-COF and Re_3-Py-2CN-COF.

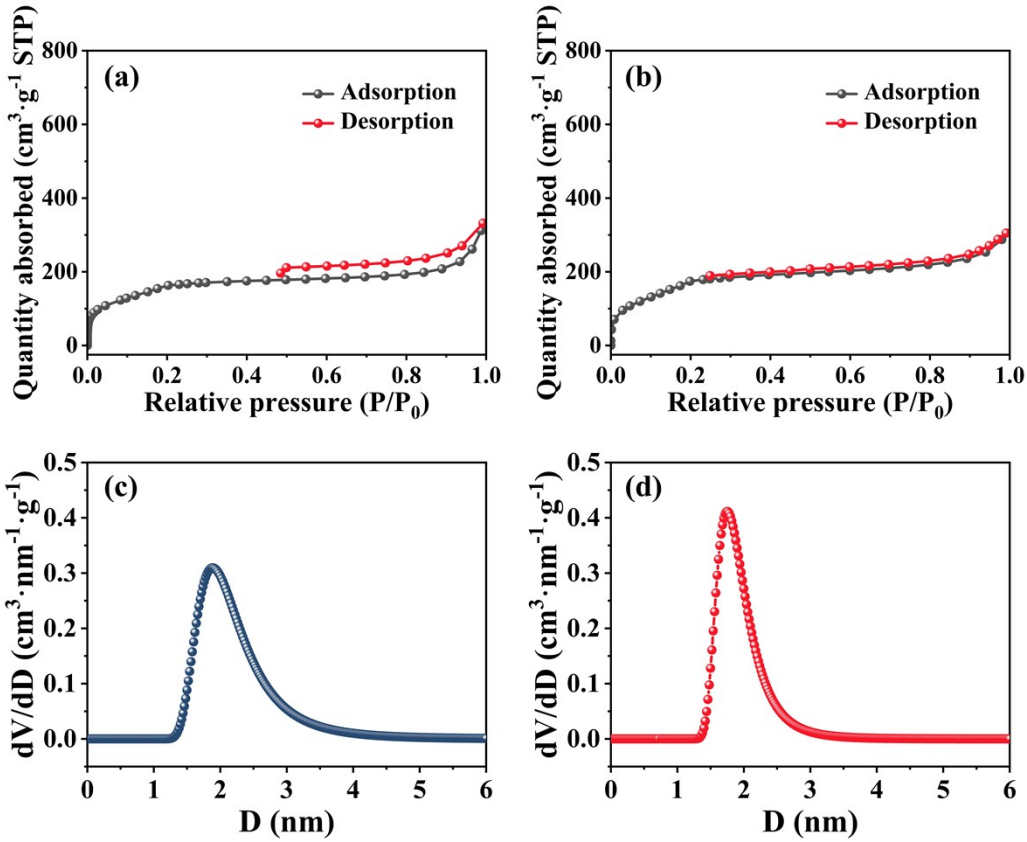

Fig. S4. The nitrogen adsorption-desorption isotherm curves of (a) Py-2CN-COF (b) Re_3-Py-2CN-COF and the pore size distribution plots of (c) Py-2CN-COF (d) Re_3-Py-2CN-COF.

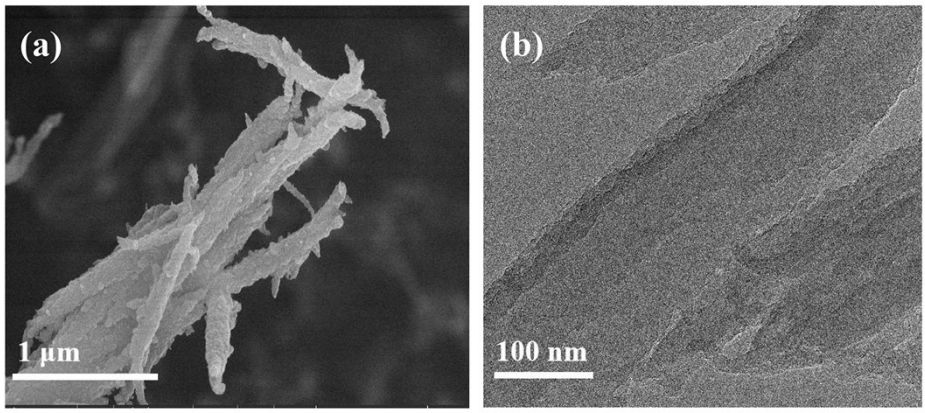

Fig. S5. (a) The SEM and (b) TEM images of Py-2CN-COF.

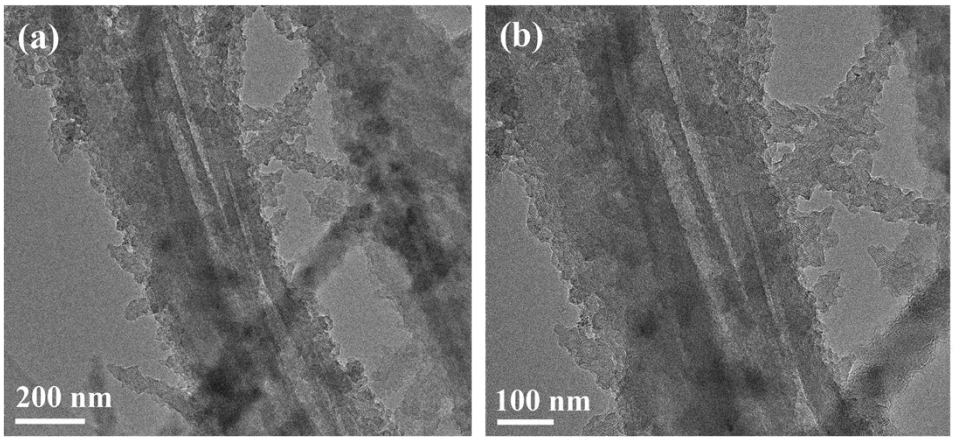

Figure. S6. (a,b) TEM images of Re_5-Py-2CN-COF at different magnifications.

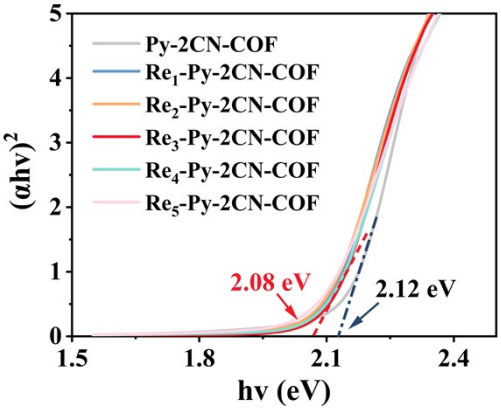

Fig. S7. The tauc plot of Py-2CN-COF and Re_x-Py-2CN-COF (x = 1, 2, 3, 4, 5).

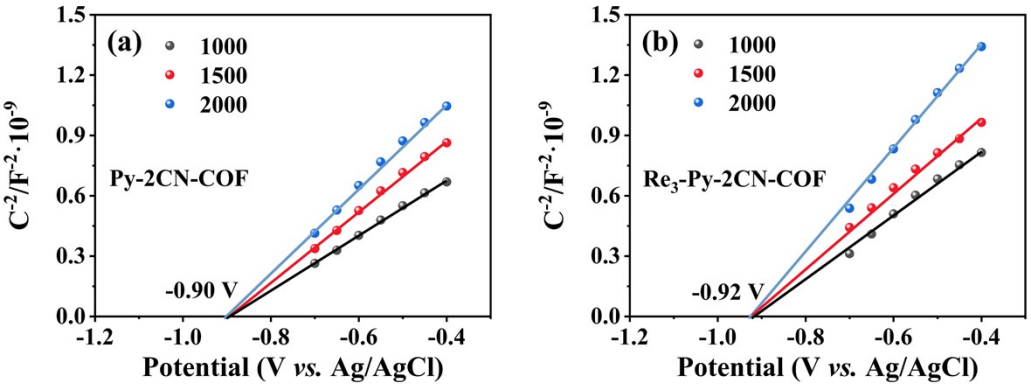

Fig. S8. The Mott-Schottky plots of (a) Py-2CN-COF and (b) Re_3-Py-2CN-COF.

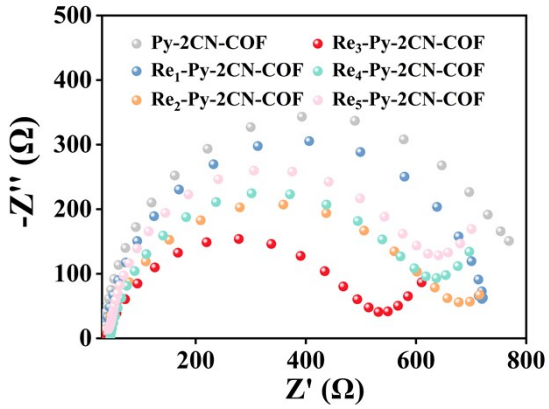

Fig. S9. The EIS plot of Py-2CN-COF and Re_x-Py-2CN-COF (x = 1, 2, 3, 4, 5).

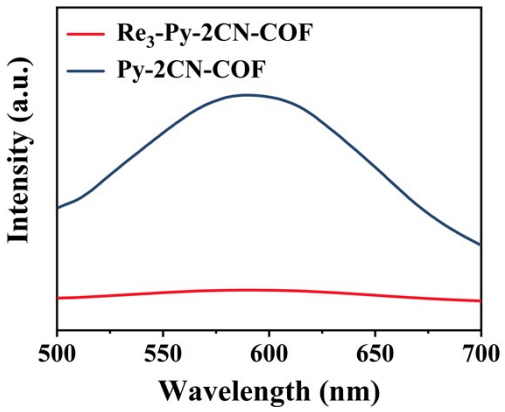

Fig. S10. Steady-state PL spectroscopy of Py-2CN-COF and Re_3-Py-2CN-COF.

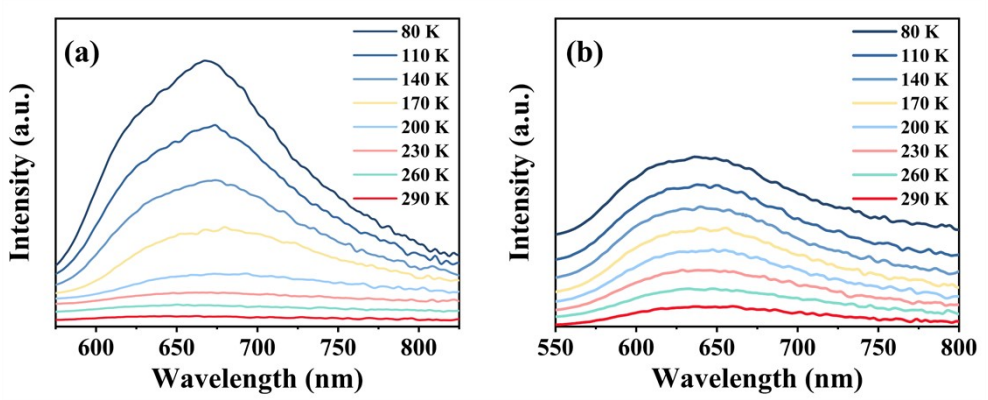

Fig. S11. TDPL spectra with excitation wavelength at 420 nm of (a) Py-2CN-COF and (b) Re_3-Py-2CN-COF.

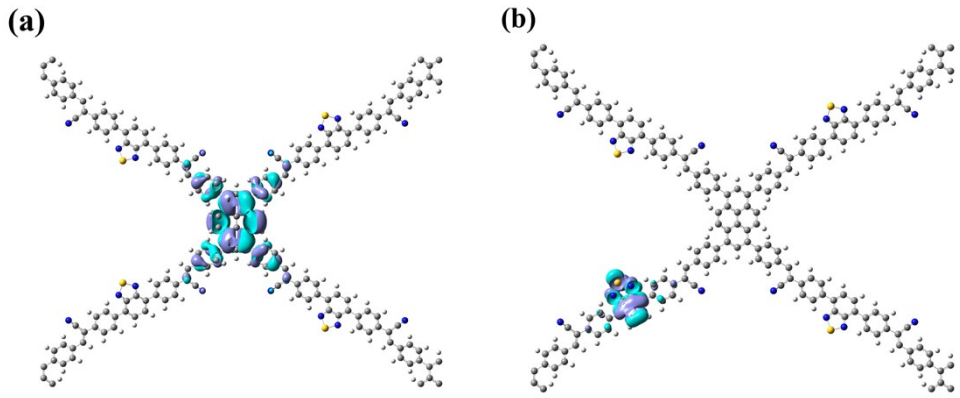

Fig. S12. The (a) HOMO and (b) LUMO orbital diagrams of Py-2CN-COF.

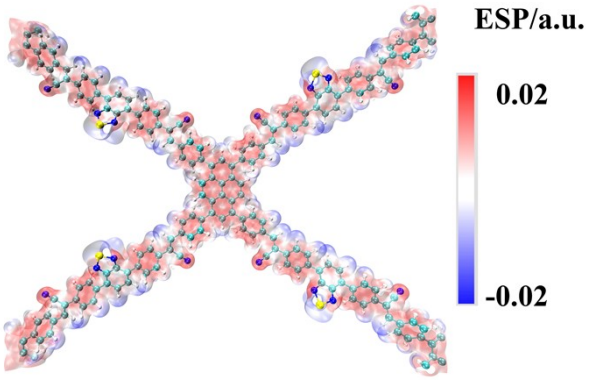

Fig. S13. The ESP plot of Py-2CN-COF.

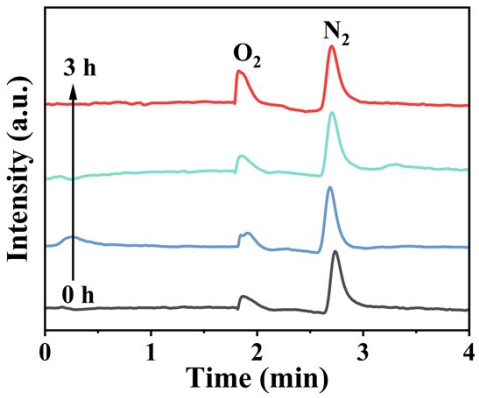

Fig. S14. The O_2 and N_2 peak plots of Re_3-Py-2CN-COF under the photocatalytic CO_2 reduction.

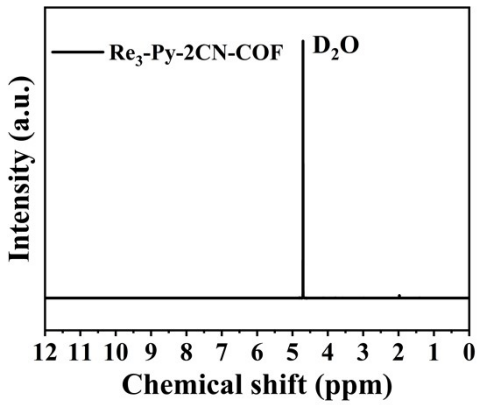

Fig. S15. ^{1}H NMR spectrum of the liquid product of CO_2RR by Re_3-Py-2CN-COF.

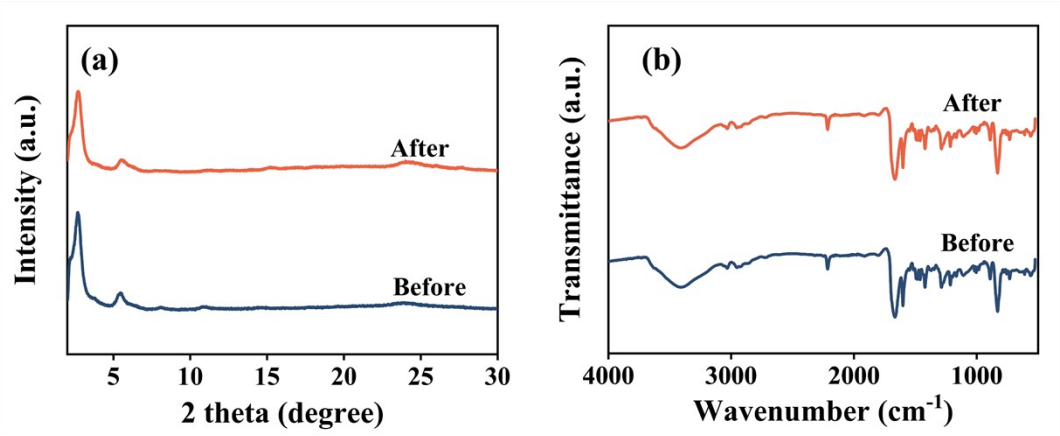

Fig. S16. (a) The PXRD pattern and (b) FT-IR spectra of samples before and after the reaction.

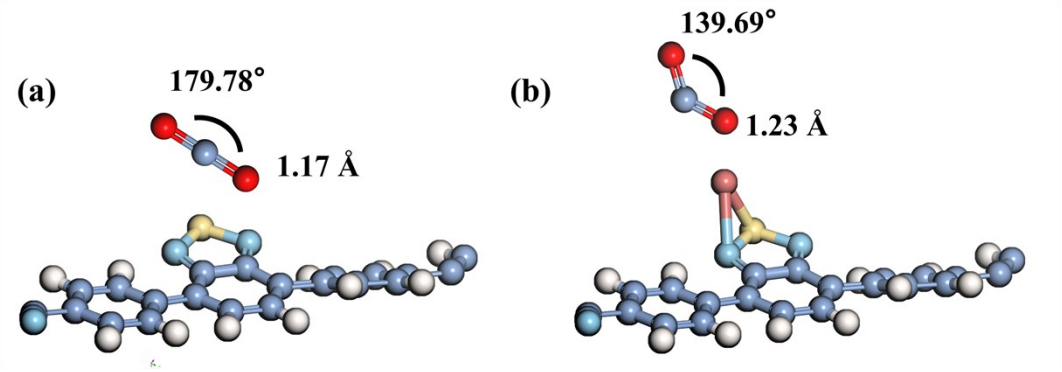

Fig. S17. The adsorption configuration of (a) Re_3-Py-2CN-COF and (b) Py-2CN-COF.

Table. S1. The BET surface area and pore size of Py-2CN-COF and Re_3-Py-2CN-COF.

Catalysts	BET surface area (m^2/g)	Pore size (nm)
Py-2CN-COF	666.07	1.88
Re_3-Py-2CN-COF	603.35	1.76

Table. S2. The selectivity of products of Py-2CN-COF and Re_x-Py-2CN-COF (x =1, 2, 3, 4, 5) from CO_2.

Catalysts	CO (%)	CH_4 (%)
Py-2CN-COF	85.5	14.5
Re_1-Py-2CN-COF	90.6	9.4
Re_2-Py-2CN-COF	91.2	8.8
Re_3-Py-2CN-COF	92.3	7.7
Re_4-Py-2CN-COF	92.0	8.0
Re_5-Py-2CN-COF	91.3	8.7

Table S3. Summary of recently reported photocatalytic CO_2 reduction properties of photocatalysts.

Photocatalysts	Products	Conditions	Yield rate ($\mu mol^{-1} \cdot g^{-1} \cdot h^{-1}$)	Light	Ref.
Re_3-Py-2CN-COF	CO	Ionic Liquid/H_2O	119.5	λ ≥ 420 nm	This work
BTT-bpy-COF-Re	CO	H_2O	110.9	λ ≥ 420 nm	1
COF-Co-N_4	CO	H_2O	110.3	λ ≥ 420 nm	2
Mn_1/PCN-N_V	CO	H_2O	29.63	λ ≥ 420 nm	3
Ni-tp-COF	CO	H_2O	15.0	λ ≥ 420 nm	4
CuDAPP-TP-COF	CO	H_2O	47.1	λ ≥ 420 nm	5
$Ce(tmhd)_4$	CO	$Ru(bpy)_3Cl_2$	86	λ ≥ 420 nm	6
CHt/V_S-ZIS	CO	H_2O	73.3	λ ≥ 420 nm	7
Cu-Bpy-COF	CH_4	TEA、H_2O	70	λ ≥ 420 nm	8
AuNPs@SiO_2-AuNCs	CO	H_2O	64.8	λ ≥ 420 nm	9
N_3-COF-MoS_2	CO	H_2O	28	λ ≥ 420 nm	10

References

1. H. Dong, H. Che, L. Bai, N. Zhang, Y. Tian, B. Li, Y. Wang, X. Zhang and F. Zhang, *Inorg. Chem.*, 2024, **63**, 24421-24428.
2. S. Xia, Y. Liu, R. Zhu, J. Feng, W. Han and Z. Gu, *Macromol. Rapid Commun.*, 2025, **46**, e2400780.
3. H. Zhao, R. Bi, M. Ju, H. Wang, R. Chen, X. Zhu and Q. Liao, *J. Phys. Chem. Lett.*, 2025, **16**, 9370-9380.
4. P. Wang, Y. Dai, Z. Song, Y. Wang, J. Wei, Z. Liu, Y. Ma, F. Yang, J. Qu, S. Liu, Y. Cai, X. Yang, C. Li and J. Hu, *Chem. Eng. J.*, 2025, **511**, 162084.
5. Y. Hou, H. Ma, D. Zhu, R. Li, Z. Zhao, C. Li, C. Cui and J. Wang, *Dalton Trans.*, 2024, **54**, 405-413.
6. Y. Zhao, J. Zhang, H. Wang, R. Zhang, Y. Teng, M. Li, Y. Song and Z. Tan, *Chem. Commun.*, 2024, **60**, 12433-12436.
7. S. Yuan, Y. Feng, S. Liang, Y. Zhang, J. Zhao, Y. Wang, P. Yang and Q. Gu, *Mater. Today Energy*, 2025, **48**, 101814.
8. Y. Zhang, L. Cao, G. Bai and X. Lan, *Small*, 2023, **19**, e2300035.
9. J. Fang, J. Li, Y. Chen, J. Cheng, C. Zhu and J. Mao, *Inorg. Chem.*, 2024, **63**, 19375-19381.
10. J. Ning, Q. Niu, Z. Liu and L. Li, *Green Chem.*, 2025, **27**, 6804-6812.